Impact-contact dynamics in a disc-ball system

Caishan Liu, Hongjian Zhang, Zhao Zhen, Bernard Brogliato

Impact–contact dynamics in a disc–ball system

Caishan Liu[1], Hongjian Zhang[1], Z h e n Z h a o [2] and Bernard Brogliato[3]

[1]State Key Laboratory for Turbulence and Complex Systems,
College of Engineering, Peking University, Beijing 100871,
People's Republic of China
[2]School of Aeronautic Science and Engineering, Beihang University,
Beijing 100191, People's Republic of China
[3]INRIA, BIPOP Project Team, ZIRST Montbonnot, 655 avenue de
l'Europe, 38334 Saint Ismier, France

This paper concerns a disc–ball system, in which a moving ball collides against a disc resting on a rough, fixed horizontal surface. The complexity in such a simple object is due to the presence of the line contact between the disc and the fixed plate, which significantly influences the impact-generated state of the disc. We deal with this problem in a uniform framework that encapsulates different structures of the mathematical model, including contacts, impacts, stick–slip in friction, as well as the transitions among different states of the variable-structure dynamics. We design specific experiments that provide useful information to help determine the macroscopic parameters in impact and friction. Other complicated cases concerned with the couplings between impacts and friction are theoretically and experimentally investigated. Excellent agreements between numerical and experimental results support our theoretical developments.

Keywords:
line contact, multiple impacts, Coulomb's
friction, stick–slip

1. Introduction

Methods confined in rigid-body dynamics to deal with contact–impact phenomena are, in general, classified into the following categories: (i) constraint equations for the representation of the geometrical interfaces [1–3] and (ii) compliance models with constitutive equations for reflecting the interactions between bodies [4,5]. The first kind mainly concerns large-scale responses, regardless of the local deformation on interfaces. The second kind depends on specific constitutive equations to

provide contact forces [6]. Even though both methods can provide adequate solutions in a variety of scientific and engineering applications, the presence of friction on interfaces complicates the dynamics and continues to pose modelling problems [7–9].

The main difficulty in using constraint methods is that the incompatibilities among different constraint equations manifest singularity [10]. Examples are easily found in indeterminate problems, where the unknown quantities relating to constraints cannot be fully solved, and in the Painlevé paradox, where the rigidity condition of contacting bodies, under certain conditions, is not fully compatible with Coulomb's friction law [11–14]. Although compliance methods can essentially get rid of these singularities, the presence of small scales for deformation as well as the artificial selection for model parameters without a clear criterion also results in difficulties in simulations, especially in dealing with impacts and friction. In this situation, the interplay on contact interfaces finishes in an extremely short time interval, and the energy residing on the surfaces usually evolves rapidly and dissipates to some extent.

To avoid the complexity of modelling the dissipation in impact processes, the coefficient of restitution is a common concept widely accepted in impact dynamics. However, its original definitions from both Newton and Poisson only focus on a single impact without friction, which are well known to be unsuitable for frictional impacts [15,16]. Establishing the dissipation at an energy level, proposed by Stronge [5], has been thoroughly acknowledged in the academic field of impact dynamics. Nevertheless, the energetic definition requires an analysis for the impact process. When several contact points are simultaneously presented in impacts, mathematical models should have the ability to reflect the dispersion effects of energy. The requirements from Stronge's definition and dispersion effects in multiple impacts place impact problems in a dilemma: the local deformation is indispensable in impact models, but its presence usually results in the solutions being sensitive to the parameters adopted in compliance models [17,18].

To solve the above problem in a simple way without resorting to local deformation, a comprehensive framework was established in our previous papers [19,20], and was validated by a variety of applications [20–22]. Different from Darboux–Keller impact dynamics [23,24], which only concerns a single impact point coupled with friction, the main idea of our theory is that the evolution of energy during impacts can be governed by a set of impulsive differential equations with respect to a 'time-like' independent normal impulse. Meanwhile, dissipation of energy in impacts is localized by Stronge's energetic coefficient of restitution. To focus on the dispersion effects of energy among different points, our previous studies excluded friction effects on impact interfaces.

As is well known, friction extremely complicates contact–impact problems, even if it is only a single rough point impact [25,26]. Moreover, friction itself, especially for the stick–slip transition, is still a tough issue. Recent studies [27] presented a clear physical picture that the transition between stick and slip motions exposes a complex dynamics process during an extremely small time scale. To reflect the internal dynamics confined in the tangential microscopic motion, Dankowicz [28] presented a simple model using an auxiliary internal variable to scale friction force. Recently, Eriten [29,30] developed a micro-mechanics-based friction model for flat rough contacting surfaces. By solving a single asperity contact problem, this model adopted statistical summation to capture the friction force for the representation of the macroscopic response. In this sense, the coefficients of slip and stick, existing in the regularized Coulomb friction law, are only the representation for the stable responses of the small-time-scale dynamics.

Owing to the simple expression, the regularized Coulomb friction law is widely recognized by many researchers and has been applied in a variety of mechanical systems. In this paper, we will develop the theory of multiple impacts with friction by embedding the regularized Coulomb friction law into our previous framework. It is worth noting that the ignorance of the tangential compliance in the regularized Coulomb friction model may influence the outputs of dynamics. Attention paid to these effects can be found in Jia [31] and Jia *et al*. [32].

Before the contents of the paper are fully deployed, we mention some technical details, which are subtle in developing our theory. In comparison with contact dynamics, impact models can be simplified by introducing assumptions widely accepted in shock dynamics. Therefore, except

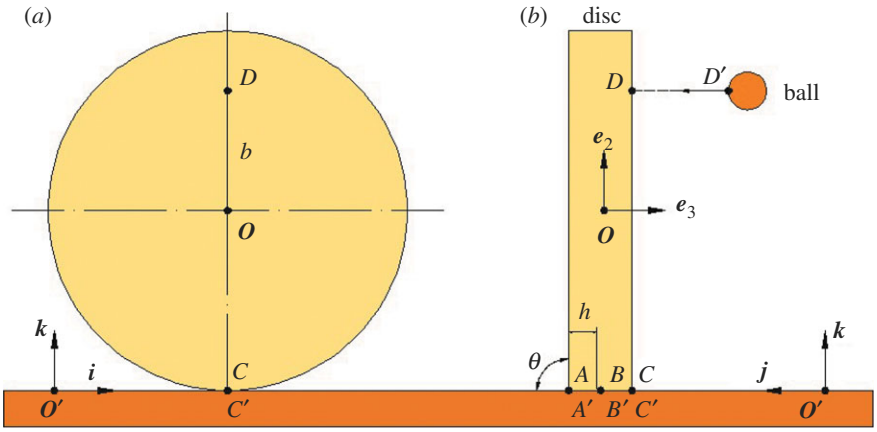

Figure 1. A disc lying on a rough surface is impacted by a moving ball. (*a*) The lateral view for the impacted surface of the disc, and (*b*) for the face view of the disc–ball system. (Online version in colour.)

that pre-treatment is required in impact dynamics, contact and impact essentially fall into the same sort of dynamic problem, and thus can be confined in a uniform mathematical model. Undoubtedly, the uniform model needs a variable structure in order to be adaptable to the various transitions induced by friction and contact, and the conditions relating to the occurrence of these transitions should be built in simulations. To give a clear picture for the subtle issues, we develop our theory using a disc–ball system, in which a moving ball collides against a disc standing vertically on a rough fixed horizontal surface. Such a simple object also allows us to easily build an apparatus for experimental validation.

The rest of this paper is organized as follows: we develop the theory of contact–impact with friction in §2, which consists of a kinematical analysis, a uniform expression for the governing equations, the determination of contact forces, impact dynamics and the transition condition between contact and impact, and a discussion for a Painlevé paradox. In §3, we introduce the experimental apparatus and the measurement methods, as well as the identification of macroscopic parameters in impact and friction. A comparison between numerical and experimental results is carried out in §4, together with an analysis for the responses of the dynamics. We conclude the paper in §5.

2. The dynamics of a disc–ball system

(a) A uniform expression for the governing equations

Figure 1 plots the disc–ball system, in which a homogeneous disc with radius r, thickness $2h$ and mass m_d, stands on a rough horizontal surface. A ball with radius r_b, mass m_b, initially takes a horizontal velocity of v_b colliding against point D in the vertical symmetry axis of the disc's surface. Neglecting the rotation of the ball ($r_\mathrm{b} \ll r$), the disc–ball system is thought of as a planar system with five degrees of freedom.

Let $(x_\mathrm{d}, y_\mathrm{d}, z_\mathrm{d})$ and $(x_\mathrm{b}, y_\mathrm{b}, z_\mathrm{b})$ (in a Galilean frame $(\boldsymbol{O}', \boldsymbol{i}, \boldsymbol{j}, \boldsymbol{k})$) be the coordinates of the mass centre of the disc and the position of the particle ball, respectively. We set $x_\mathrm{d} = x_\mathrm{b} = 0$ for the planar system, and define θ as the angle of the vertical axis of the disc to axis i ($\theta = \pi/2$ for the current configuration in figure 1), by which there exists a coordinate transformation between frame $(\boldsymbol{O}', \boldsymbol{i}, \boldsymbol{j}, \boldsymbol{k})$ and a body coordinate system $(\boldsymbol{O}, \boldsymbol{e}_1, \boldsymbol{e}_2, \boldsymbol{e}_3)$, fixed at the mass centre of the disc. The generalized coordinates of the system are selected as $\boldsymbol{q} = (y_\mathrm{b}, z_\mathrm{b}, y_\mathrm{d}, z_\mathrm{d}, \theta)^\mathrm{T}$.

Generally, the line contact between the disc and the ground forms a contact–stress distribution that complicates much of the modelling of the contact–impact dynamics. To simplify, we use three lumped points (A, B and C) with equal intervals to represent the interplay between the disc and

the horizontal surface. In impact dynamics, the potential energies residing on the three lumped points are then used to approximately reflect the evolution of the simultaneous spatial stresses on the line-contact interface. This treatment is not rigorous, but the three-point model may of a straightforward way of dealing with the line contact confined in the thin disc.

Under the simplification, the disc–ball system consists of four potential contact sets $i = \{i, i'\}$, $i = A, B, C, D$, where the element without a prime ($'$) refers to the point on the disc, whereas the other element is related to the point on other contacting bodies. Let $\boldsymbol{\delta} = (\delta_A, \delta_B, \delta_C, \delta_D)^{\mathrm{T}}$ be the relative normal displacements. In terms of geometrical relationships, they are easily expressed as

$$\left.\begin{aligned} \delta_A(\boldsymbol{q}) &= z_{\mathrm{d}} - (hc + rs), \\ \delta_B(\boldsymbol{q}) &= z_{\mathrm{d}} - rs, \\ \delta_C(\boldsymbol{q}) &= z_{\mathrm{d}} + (hc - rs) \\ \text{and} \qquad \delta_D(\boldsymbol{q}) &= (z_{\mathrm{b}} - z_{\mathrm{d}})c - (y_{\mathrm{b}} + r_{\mathrm{b}} - y_{\mathrm{d}})s - h, \end{aligned}\right\} \tag{2.1}$$

where symbols s and c are the abbreviations for $\sin\theta$ and $\cos\theta$, respectively. The time rate of change of δ_i in a matrix notation is

$$\dot{\boldsymbol{\delta}} = [\boldsymbol{W}_A, \boldsymbol{W}_B, \boldsymbol{W}_C, \boldsymbol{W}_D]^{\mathrm{T}}\dot{q} = \boldsymbol{W}^{\mathrm{T}}(\boldsymbol{q})\dot{\boldsymbol{q}}, \tag{2.2}$$

where $\dot{\boldsymbol{\delta}} = (\dot{\delta}_A, \dot{\delta}_B, \dot{\delta}_C, \dot{\delta}_D)^{\mathrm{T}}$, and $\boldsymbol{W}^{\mathrm{T}}(\boldsymbol{q})$ is a transformation matrix for the relative velocities $\dot{\delta}_i$ with respect to the generalized velocities $\dot{\boldsymbol{q}}$,

$$\boldsymbol{W}(\boldsymbol{q}) = \begin{bmatrix} 0 & 0 & 0 & -s \\ 0 & 0 & 0 & c \\ 0 & 0 & 0 & s \\ 1 & 1 & 1 & -c \\ hs - rc & -rc & -hs - rc & -b \end{bmatrix}. \tag{2.3}$$

where b is the vertical distance of the impact point D to the symmetrical axis of the disc parallel to the horizontal plane.

The relative velocities among potential contact points $\boldsymbol{v}_i^r$ can be decomposed into the components along their normal ($\boldsymbol{n}_i$) and tangential ($\boldsymbol{\tau}_i$) directions, respectively,

$$\boldsymbol{v}_i^r = v_i^\tau \boldsymbol{\tau}_i + \dot{\delta}_i \boldsymbol{n}_i, \tag{2.4}$$

where $\boldsymbol{\tau}_i$ is a unit vector for the slip direction at contact i,

$$\boldsymbol{\tau}_i = \frac{\boldsymbol{v}_i^r - \dot{\delta}_i \boldsymbol{n}_i}{\|\boldsymbol{v}_i^r - \dot{\delta}_i \boldsymbol{n}_i\|}. \tag{2.5}$$

For the planar disc–ball system, we can define $\boldsymbol{\tau}_A = \boldsymbol{\tau}_B = \boldsymbol{\tau}_C = \boldsymbol{j}$ and $\boldsymbol{\tau}_D = \boldsymbol{e}_2$. Thus, the relative tangential velocities in a matrix notation are expressed as

$$\boldsymbol{v}^\tau = [\boldsymbol{N}_A, \boldsymbol{N}_B, \boldsymbol{N}_C, \boldsymbol{N}_D]^{\mathrm{T}} = \boldsymbol{N}(\boldsymbol{q})^{\mathrm{T}}\dot{\boldsymbol{q}}, \tag{2.6}$$

where $\boldsymbol{v}^\tau = (v_A^\tau, v_B^\tau, v_C^\tau, v_D^\tau)^{\mathrm{T}}$ and

$$\boldsymbol{N}(\boldsymbol{q}) = \begin{bmatrix} 0 & 0 & 0 & -c \\ 0 & 0 & 0 & -s \\ 1 & 1 & 1 & c \\ 0 & 0 & 0 & s \\ (hc + rs) & rs & -(hc - rs) & -h \end{bmatrix}. \tag{2.7}$$

In terms of equations (2.2) and (2.6), the time rate of the relative normal and tangential velocities is expressed as

$$\ddot{\boldsymbol{\delta}} = \boldsymbol{W}^{\mathrm{T}}(\boldsymbol{q})\ddot{\boldsymbol{q}} + \boldsymbol{S}^n(\boldsymbol{q}, \dot{\boldsymbol{q}}) \tag{2.8}$$

and

$$\dot{\boldsymbol{v}}^\tau = \boldsymbol{N}^{\mathrm{T}}(\boldsymbol{q})\ddot{\boldsymbol{q}} + \boldsymbol{S}^\tau(\boldsymbol{q}, \dot{\boldsymbol{q}}), \tag{2.9}$$

where $\boldsymbol{S}^n(\boldsymbol{q},\dot{\boldsymbol{q}}) = \dot{\boldsymbol{W}}(\boldsymbol{q},\dot{\boldsymbol{q}})^{\mathrm{T}}\dot{\boldsymbol{q}}$, $\boldsymbol{S}^\tau(\boldsymbol{q},\dot{\boldsymbol{q}}) = \dot{\boldsymbol{N}}(\boldsymbol{q},\dot{\boldsymbol{q}})^{\mathrm{T}}\dot{\boldsymbol{q}}$. Equations (2.8) and (2.9) consist of kinematical relationships that should be satisfied by the (potential) contact points in contacting bodies.

The kinetic energy of the disc–ball system $T(\boldsymbol{q},\dot{\boldsymbol{q}})$ is given by $T(\boldsymbol{q},\dot{\boldsymbol{q}}) = T_{\mathrm{b}}(\boldsymbol{q},\dot{\boldsymbol{q}}) + T_{\mathrm{d}}(\boldsymbol{q},\dot{\boldsymbol{q}}) = \frac{1}{2}m_{\mathrm{b}}\dot{y}_{\mathrm{b}}^2 + \frac{1}{2}m_{\mathrm{b}}\dot{z}_{\mathrm{b}}^2 + \frac{1}{2}m_{\mathrm{d}}\dot{y}_{\mathrm{d}}^2 + \frac{1}{2}m_{\mathrm{d}}\dot{z}_{\mathrm{d}}^2 + \frac{1}{2}I\dot{\theta}^2$ and $I = \frac{1}{4}m_{\mathrm{d}}r^2 + \frac{1}{3}m_{\mathrm{d}}h^2$. By selecting the horizontal ground as the zero-potential surface, the potential energy is $U(\boldsymbol{q}) = m_{\mathrm{b}}gz_{\mathrm{b}} + m_{\mathrm{d}}gz_{\mathrm{d}}$.

To describe the interaction at a contact set i, we separate the action and reaction forces into the components along the normal and tangential directions, $\boldsymbol{F}_i = F_i^n\boldsymbol{n}_i + F_i^\tau\boldsymbol{\tau}_i$ and $\boldsymbol{F}_{i'} = -\boldsymbol{F}_i = -F_i^n\boldsymbol{n}_i - F_i^\tau\boldsymbol{\tau}_i$. The virtual works done by the contact forces are given by

$$\delta w_i^n = F_i^n\boldsymbol{n}_i\cdot\delta\boldsymbol{r}_i - F_i^n\boldsymbol{n}_i\cdot\delta\boldsymbol{r}_{i'} = F_i^n[(\delta\boldsymbol{r}_i - \delta\boldsymbol{r}_{i'})\cdot\boldsymbol{n}_i] \tag{2.10}$$

and

$$\delta w_i^\tau = F_i^\tau\boldsymbol{\tau}_i\cdot\delta\boldsymbol{r}_i - F_i^\tau\boldsymbol{\tau}_i\cdot\delta\boldsymbol{r}_{i'} = F_i^\tau[(\delta\boldsymbol{r}_i - \delta\boldsymbol{r}_{i'})\cdot\boldsymbol{\tau}_i], \tag{2.11}$$

where $\delta\boldsymbol{r}_i$ and $\delta\boldsymbol{r}_{i'}$ are the virtual displacements corresponding to the pair of contact forces. Once all the rough contacts are represented by interaction forces, the system only suffers holonomic constraints admitting the following equalities: $\partial\boldsymbol{r}_i/\partial q_j = \partial\dot{\boldsymbol{r}}_i/\partial\dot{q}_j$. Therefore,

$$\delta\boldsymbol{r}_i - \delta\boldsymbol{r}_{i'} = \sum_{j=1}^{5}\left(\frac{\partial\boldsymbol{r}_i}{\partial q_j} - \frac{\partial\boldsymbol{r}_{i'}}{\partial q_j}\right)\delta q_j = \sum_{j=1}^{5}\left(\frac{\partial\dot{\boldsymbol{r}}_i}{\partial\dot{q}_j} - \frac{\partial\dot{\boldsymbol{r}}_{i'}}{\partial\dot{q}_j}\right)\delta q_j = \sum_{j=1}^{5}\left(\frac{\partial\boldsymbol{v}_i^r}{\partial\dot{q}_j}\right)\delta q_j. \tag{2.12}$$

The virtual work done by the pair of contact forces is then expressed as

$$\left.\begin{aligned}\delta w_i^n &= F_i^n\sum_{j=1}^{5}\frac{\partial(\boldsymbol{v}_i^r\cdot\boldsymbol{n}_i)}{\partial\dot{q}_j}\delta q_j = F_i^n\sum_{j=1}^{5}\frac{\partial\dot{\delta}_i}{\partial\dot{q}_j}\delta q_j\\ \text{and}\qquad \delta w_i^\tau &= F_i^\tau\sum_{j=1}^{5}\frac{\partial(\boldsymbol{v}_i^r\cdot\boldsymbol{\tau}_i)}{\partial\dot{q}_j}\delta q_j = F_i^\tau\sum_{j=1}^{5}\frac{\partial v_i^\tau}{\partial\dot{q}_j}\delta q_j.\end{aligned}\right\} \tag{2.13}$$

Defining a Lagrangian function $L = T - U$ and using Euler–Lagrange equations, the dynamics of the system is governed by

$$\boldsymbol{M}\ddot{\boldsymbol{q}} = \boldsymbol{G} + \boldsymbol{W}(\boldsymbol{q})\boldsymbol{F}^n + \boldsymbol{N}(\boldsymbol{q})\boldsymbol{F}^\tau, \tag{2.14}$$

where $\boldsymbol{M} = \mathrm{diag}(m_{\mathrm{b}}, m_{\mathrm{b}}, m_{\mathrm{d}}, m_{\mathrm{d}}, I) \in \mathbb{R}^{5\times5}$, $\boldsymbol{G} = [0, -m_{\mathrm{b}}g, 0 - m_{\mathrm{d}}g, 0]^{\mathrm{T}}$, $\boldsymbol{F}^n = [F_A^n, F_B^n, F_C^n, F_D^n]^{\mathrm{T}}$, $\boldsymbol{F}^\tau = [F_A^\tau, F_B^\tau, F_C^\tau, F_D^\tau]^{\mathrm{T}}$.

To obtain solutions for equation (2.14), we must determine the contact forces $\boldsymbol{F}^n$ and $\boldsymbol{F}^\tau$. Basically, they can be calculated by either introducing constraint equations, or inserting compliance models, for the contacts involved in the system.

(b) Determination of contact forces

Notice that equations (2.8) and (2.9) are the kinematical relationships that must be satisfied by contacts. We can combine them with equation (2.14) to establish the equations that govern the local dynamics of the contacts,

$$\ddot{\boldsymbol{\delta}} = \boldsymbol{W}^{\mathrm{T}}\boldsymbol{M}^{-1}\boldsymbol{W}\boldsymbol{F}^n + \boldsymbol{W}^{\mathrm{T}}\boldsymbol{M}^{-1}\boldsymbol{N}\boldsymbol{F}^\tau + \boldsymbol{W}^{\mathrm{T}}\boldsymbol{M}^{-1}\boldsymbol{G} + \boldsymbol{S}^n \tag{2.15}$$

and

$$\dot{\boldsymbol{v}}^\tau = \boldsymbol{N}^{\mathrm{T}}\boldsymbol{M}^{-1}\boldsymbol{W}\boldsymbol{F}^n + \boldsymbol{N}^{\mathrm{T}}\boldsymbol{M}^{-1}\boldsymbol{N}\boldsymbol{F}^\tau + \boldsymbol{N}^{\mathrm{T}}\boldsymbol{M}^{-1}\boldsymbol{G} + \boldsymbol{S}^\tau. \tag{2.16}$$

Let us introduce geometrical constraints relating to the non-penetrating condition for considering the interplay on the contact interfaces. In this case, there exist complementarity relationships between the normal relative displacements and the contact forces,

$$\delta_i(t)\cdot F_i^n(t) = 0, \quad \delta_i(t) \geq 0,\ F_i^n(t) \geq 0,\ i = A, B, C, D. \tag{2.17}$$

For a closed contact set, one has a constraint equation $\delta_i(t) = 0$. Owing to the unilateral property of contacts, however, the constraint established at the level of displacement is insufficient

to determine constraint forces. Therefore, we have to resort to a complementarity relationship built at the velocity level,

$$\dot{\delta}_i(t) \cdot F_i^n(t) = 0, \quad \dot{\delta}_i(t) \geq 0,\ F_i^n(t) \geq 0,\ i = A, B, C, D. \tag{2.18}$$

Explanations for (2.18) are as follows: if $\dot{\delta}_i(t) > 0$, equation (2.18) clearly indicates that the contact force is $F_i^n(t) = 0$, while $\dot{\delta}_i(t) < 0$, the non-penetrating condition is violated, thus impact occurs on the interface. If $\dot{\delta}_i(t) = 0$, a weak interaction with $F_i^n(t) \geq 0$ may be excited. However, the existence of a corner point $(0, 0)$ in equation (2.18) means that the contact force is indeterminate, thus a high-order differential is required,

$$\ddot{\delta}_i(t) \cdot F_i^n(t) = 0, \quad \ddot{\delta}_i(t) \geq 0, \quad F_i^n(t) \geq 0, \quad i = A, B, C, D. \tag{2.19}$$

The combination of equations (2.17–2.19) gives an integrated way for distinguishing the normal contact force and the contact state at each contact set.

For the rough contacts, Coulomb friction law specifies that the tangential and normal components of the contact forces should satisfy the following relationship characterized by two coefficients:

$$F_i^\tau = \begin{cases} -\mu_i F_i^n \operatorname{sign}(\boldsymbol{\tau}_i), & \text{if } v_i^\tau \neq 0, \text{ sliding state,} \\ \leq \mu_i^s F_i^n, & \text{if } v_i^\tau = 0, \text{ sticking state,} \end{cases} \tag{2.20}$$

where $\mu_i > 0$ and $\mu_i^s > \mu_i$ are the slip and stick friction coefficients at contact point i, respectively. If $v_i^\tau \neq 0$, the force of friction F_i^τ opposes motion and has magnitude $\mu_i F_i^n$. In the case of $v_i^\tau = 0$, however, the force of friction F_i^τ is unknown, thus a supplementary condition should be provided.

Similar to the analysis for the normal interaction, the condition $v_i^\tau = 0$, which is necessary for a stick–slip transition, means that a constraint exists in the tangential motion. Therefore, a relationship between the normal and tangential forces can be obtained by the differential form of the tangential velocity constraint

$$\dot{v}_i^\tau = \boldsymbol{N}_i^{\mathrm{T}}(\boldsymbol{q})\ddot{\boldsymbol{q}} + \boldsymbol{S}_i^\tau(\boldsymbol{q}, \dot{\boldsymbol{q}}) = 0, \quad \text{if } v_i^\tau = 0,\ \delta_i = 0,\ \dot{\delta}_i = 0. \tag{2.21}$$

If no singularities arise in the rigid-body model, friction forces $\boldsymbol{F}^\tau$ can always be expressed as functions relative of $\boldsymbol{F}^n$. By substituting these relationships into the local dynamics (2.15) and (2.16), and using the complementarity condition shown in (2.19), the solutions of the contact forces $\boldsymbol{F}^n$ and $\boldsymbol{F}^\tau$ are obtained.

It is worth noting that stick–slip transition at $v_i^\tau = 0$ is limited by an upper bound μ_i^s. Therefore, a slip motion is transferred into a stick state at $v_i^\tau = 0$ only if the ratio of F_i^n and F_i^τ, which is obtained by setting $\dot{v}_i^\tau = 0$, satisfies $F_i^\tau / F_i^n \leq \mu_i^s$. Similarly, a transition from a stick state to a slip state occurs only if $F_i^\tau / F_i^n > \mu_i^s$. In the latter case, the subsequent slip direction is assumed to be consistent with the one of the maximum static friction force obtained from the condition $\dot{v}_i^\tau = 0$ [5,25].

Another way of determining contact forces is the method of inserting compliance into the contact interfaces. For non-adhesion material, the compliance model is usually represented by a constitutive equation of the following form:

$$F_i^n(\delta_i) = \begin{cases} f_i(-\delta_i), & \text{if } \delta_i \leq 0, \text{ contact state,} \\ 0, & \text{if } \delta_i > 0, \text{ separating state,} \end{cases} \tag{2.22}$$

where $f_i(-\delta_i)$ is a general function with respect to the compressional deformation. In this case, the solutions of the system are achieved by substituting the compliance model together with Coulomb's friction law into the governing equation (2.14) and the local dynamics in equations (2.15) and (2.16). The advantage of using compliance models is that the gross motion of the system, together with local deformation, can be obtained simultaneously. Owing to the couplings among different scales, however, this method often requires a suitable numerical scheme capable of handling stiff problems in ordinary differential equations.

(c) Impact dynamics in the disc–ball system

To solve the impacts in the disc–ball system, we extend the theory in Liu *et al.* [19] to the case of impacts with friction. Under the assumptions of shock dynamics, together with the definitions for the infinitesimal impulses in the normal, $\mathrm{d}\boldsymbol{P}^n = \boldsymbol{F}^n\,\mathrm{d}t$, and in the tangential $\mathrm{d}\boldsymbol{P}^\tau = \boldsymbol{F}^\tau\,\mathrm{d}t$, equation (2.14) is then rewritten as

$$\boldsymbol{M}\,\mathrm{d}\dot{\boldsymbol{q}} = \boldsymbol{W}\,\mathrm{d}\boldsymbol{P}^n + \boldsymbol{N}\,\mathrm{d}\boldsymbol{P}^\tau. \tag{2.23}$$

The variation of the elastic potential energy $\mathrm{d}E_i$ induced by the work $\mathrm{d}w_i^n$ done by the elastic force F_i^n through a small elastic deformation $\mathrm{d}\delta_i$ is expressed as $\mathrm{d}E_i = \mathrm{d}w_i^n = -F_i^n \cdot \mathrm{d}\delta_i$, and can be rewritten as $\mathrm{d}E_i = -\dot{\delta}_i\,\mathrm{d}P_i^n$. Notice that P_i^n is always positive and increases monotonically if contact is retained. The negative work done by the normal contact force in a compressional phase of normal motion ($\dot{\delta}_i < 0$) means that the potential energy increases gradually. While in an expansion phase ($\dot{\delta}_i > 0$), the positive work results in a decrease of the potential energy. Supposing that $E_i(0) = 0$ at $P_i^n = 0$, the potential energy E_i at the instant of P_i^n is expressed as

$$E_i = -\int_0^{P_i^n} \dot{\delta}_i\,\mathrm{d}P_i^n > 0. \tag{2.24}$$

Let the constitutive equation of the compliance be a power form, $F_i^n(\delta_i) = k_i(-\delta_i)^{\alpha_i}$, where k_i is the contact stiffness at contact point i, and the minus sign means that $(-\delta_i) > 0$ when contact holds at point i. The time rate of F_i^n is expressed as

$$\frac{\mathrm{d}F_i^n}{\mathrm{d}t} = -\alpha_i k_i(-\delta_i)^{(\alpha_i-1)}\dot{\delta}_i. \tag{2.25}$$

By considering that $(-\delta_i) = (F_i^n/k_i)^{1/\alpha_i}$ and $\mathrm{d}t = \mathrm{d}P_i^n/F_i^n$, we get $(F_i^n)^{1/\alpha_i}\,\mathrm{d}F_i^n = -\alpha_i k_i^{1/\alpha_i}\dot{\delta}_i\,\mathrm{d}P_i^n$, which, by integration, yields

$$\int_0^{F_i^n} (F_i^n)^{1/\alpha_i}\,\mathrm{d}F_i^n = -\alpha_i k_i^{1/\alpha_i}\int_0^{P_i^n}\dot{\delta}_i\,\mathrm{d}P_i^n = \alpha_i k_i^{1/\alpha_i}E_i. \tag{2.26}$$

Thus, we have a relationship between the normal contact force F_i^n and the potential energy E_i,

$$F_i^n = (\alpha_i+1)^{\alpha_i/(\alpha_i+1)}k_i^{1/(\alpha_i+1)}E_i^{\alpha_i/(\alpha_i+1)}. \tag{2.27}$$

Owing to $F_i^n = \mathrm{d}P_i^n/\mathrm{d}t$, the ratio between the normal contact forces at points i and j is given by

$$\frac{F_i^n}{F_j^n} = \frac{\mathrm{d}P_i^n}{\mathrm{d}P_j^n} = \frac{(\alpha_i+1)^{\alpha_i/(\alpha_i+1)}}{(\alpha_j+1)^{\alpha_j/(\alpha_j+1)}}\frac{k_i^{1/(\alpha_i+1)}}{k_j^{1/(\alpha_j+1)}}\frac{E_i^{\alpha_i/(\alpha_i+1)}}{E_j^{\alpha_j/(\alpha_j+1)}} \triangleq R_{i,j}^n, \tag{2.28}$$

which is the distributing rule and depends only on the stiffness ratio and potential energies ratio.

Let us select a contact point j, where $E_j = \max\{E_i, i = A, B, C, D\}$, and define $\mathrm{d}P_j^n$ as a primary differential normal impulse. The normal impulses at other points can be connected with $\mathrm{d}P_j^n$ by the spatial distribution of the potential energy expressed in (2.28). The reason for selecting the point with maximum potential energy as the primary impulse $\mathrm{d}P_j^n$ is not compulsory, but can improve numerical simulations.

To reflect friction effects in the impact process, we should connect the tangential impulse $\mathrm{d}P_i^\tau$ with the primary impulse $\mathrm{d}P_j^n$. Similar to contact dynamics, the relationship between normal and tangential forces in Coulomb's friction law is equivalent to the one between the infinitesimal normal and tangential impulses in impact dynamics. By considering that the normal differential impulse has been linked with the primary impulse $\mathrm{d}P_j^n$, the governing equation (2.23) in the impact process becomes

$$\boldsymbol{M}\frac{\mathrm{d}\dot{\boldsymbol{q}}}{\mathrm{d}P_j^n} = \boldsymbol{W}\boldsymbol{R}^n + \boldsymbol{N}\boldsymbol{R}^\tau, \tag{2.29}$$

where $\boldsymbol{R}^n = [R^n_{A,j}, R^n_{B,j}, R^n_{C,j}, R^n_{D,j}]^{\mathrm{T}}$ and $\boldsymbol{R}^\tau = [R^\tau_{A,j}, R^\tau_{B,j}, R^\tau_{C,j}, R^\tau_{D,j}]^{\mathrm{T}}$ are the ratio matrices of the normal and tangential impulses relative to the primary impulse $\mathrm{d}P^n_j$.

The initial values for $\boldsymbol{R}^n(0)$ and $\boldsymbol{R}^\tau(0)$ must be provided before a simulation is launched. Let $\dot{\delta}_i(0)$ be the normal relative velocities at the beginning of impacts, and j be the closed contact set with a maximum magnitude of its normal velocity among all the closed contact sets, $|\dot{\delta}_j(0)| = \max\{|\dot{\delta}_i(0)|, \delta_i(0) = 0\}$. By multiplying $\mathrm{d}P^n_i$ together with $\dot{\delta}_i(0)$ to express the possible accumulated potential energy, $E_i(0) = -\dot{\delta}_i(0)\,\mathrm{d}P^n_i$, we base (2.28) to get

$$\frac{(\mathrm{d}P^n_i)^{1/(\alpha_i+1)}}{(\mathrm{d}P^n_j)^{1/(\alpha_j+1)}} = \frac{(\alpha_i+1)^{\alpha_i/(\alpha_i+1)}}{(\alpha_j+1)^{\alpha_j/(\alpha_j+1)}} \frac{k_i^{1/(\alpha_i+1)}}{k_j^{1/(\alpha_j+1)}} \frac{(-\dot{\delta}_i(0))^{\alpha_i/(\alpha_i+1)}}{(-\dot{\delta}_j(0))^{\alpha_j/(\alpha_j+1)}}. \tag{2.30}$$

As the 'time-like' independent variable is assigned with an initial value $\mathrm{d}P^n_j(0)$, the initial values of $\boldsymbol{R}^n(0)$ and $\boldsymbol{R}^\tau(0)$ are uniquely determined according to the above expression. Then, ratio matrices $\boldsymbol{R}^n$ and $\boldsymbol{R}^\tau$ are updated dynamically based on the evolution of the potential energies.

To correctly obtain the spatial distribution of the simultaneous potential energies among different points, the model must reflect the energy dissipation induced by either the local plastic deformation or small vibrations, or the multiple compression–expansion phases at the same contact point [19]. Supposing that the energy dissipation is counted in expansion phases, and defining η_i as the transition efficiency between potential energy $\mathrm{d}E_i$ and the work $\mathrm{d}w_i$ done by the normal contact force, we obtain

$$\mathrm{d}w_i = -\eta_i\,\mathrm{d}E_i, \quad \eta_i(\dot{\delta}_i) = \begin{cases} 1, & \text{if } \dot{\delta} \le 0, \\ e_i^2, & \text{if } \dot{\delta} > 0, \end{cases} \tag{2.31}$$

where e_i is a macroscopic parameter to encapsulate the loss of energy induced by various factors confined in a single compression–expansion cycle. Let an impact start with initial potential energy $E_i(P^{n*}_j)$, the integration of (2.31) leads to

$$E_i(P^n_j) = E_i(P^{n*}_j) - \frac{1}{\eta_i}\int_{P^{n*}_j}^{P^n_j} \dot{\delta}_i R^n_{i,j}\,\mathrm{d}P^n_j. \tag{2.32}$$

We can prove that e_i is equivalent to the definition of the energetic coefficient of restitution. Specify that $P^{n,c}_j$ is the impulse time corresponding to the end of the compressional phase, i.e. $\dot{\delta}_i(P^{n,c}_j) = 0$. In terms of equation (2.32), the potential energy at the impulse time P^n_j in an expansion phase ($\dot{\delta}_i > 0$) is given by

$$E_i(P^n_j) = E_i(P^{n,c}_j) - \frac{1}{\eta_i}\int_{P^{n,c}_j}^{P^n_j} \dot{\delta}_i R^n_{i,j}\,\mathrm{d}P^n_j, \quad \dot{\delta}_i > 0. \tag{2.33}$$

For an impact finishing in a single compression–expansion cycle with a final normal impulse $P^{n,f}_j$, we apply $E_i(P^{n,f}_j) = 0$ into equation (2.33), then get

$$\eta_i = \frac{\int_{P^{n,c}_j}^{P^{n,f}_j} \dot{\delta}_i R^n_{i,j}\,\mathrm{d}P^n_j}{E_i(P^{n,c}_j)} = -\frac{\int_{P^{n,c}_i}^{P^{n,f}_i} \dot{\delta}_i\,\mathrm{d}P^n_i}{\int_0^{P^{n,c}_i} \dot{\delta}_i\,\mathrm{d}P^n_i} = e_i^2. \tag{2.34}$$

Equation (2.34) indicates that the transition efficiency η_i agrees with the definition of the energetic coefficient of restitution. For a fully elastic impact, in which $e_i = 1$, the energy absorbed in the contact set can be completely released through expansion phases without dissipation. If $0 < e_i < 1$, part of the energy is dissipated owing to the impact process. For the specific case $e_i = 0$, which corresponds to a fully plastic impact at the contact set, the limitation of $E_i(P^n_j) \ge 0$ implies that all the energy absorbed in compressional phases will sharply disappear when the compressional phase is completed and the expansion phase vanishes. Then, the impact at that point finishes with a conglutinate state.

(d) Finite-time singularity and the Painlevé paradox

Owing to gravity, a sequence of single impacts becomes a contact state after a finite time interval. This phenomenon is often termed as 'finite-time singularity'. To find a condition that could quantify the transition, let us consider the dynamics of the disc contacting on the fixed surface at point A, whose local dynamical equation is easily obtained by using equation (2.15),

$$\frac{\mathrm{d}\dot{\delta}_A}{\mathrm{d}t} = \frac{1}{m_\mathrm{d}}F_A^n + \frac{1}{I}(hc - rs)^2 F_A^n + \frac{1}{I}(hc + rs)(hs - rc)F_A^\tau + (hc + rs)\dot{\theta}^2 - g. \tag{2.35}$$

Let T_c be a time scale relating the period of the single impact with an initial normal velocity $\dot{\delta}_A^-$, and assume that the impact only slightly changes angle θ, but the effects of non-contact forces are accounted for in the impact model. At the end of the impact, the final normal velocity $\dot{\tilde{\delta}}_A^+$ can be obtained by the integration of (2.35),

$$\frac{\dot{\tilde{\delta}}_A^+ - \dot{\delta}_A^-}{gT_\mathrm{c}} = \left(\frac{I + m_\mathrm{d}(hs - rc)^2}{m_\mathrm{d}I}\right)\frac{P_A^n}{gT_\mathrm{c}} + \frac{1}{I}(hc + rs)(hs - rc)\frac{P_A^\tau}{gT_\mathrm{c}} + \frac{(hc + rs)\dot{\theta}_m^2}{g} - 1, \tag{2.36}$$

where $\dot{\theta}_m$ is an average velocity during the time interval, and $P_A^n = \int_0^{T_\mathrm{c}} F_A^n(t)\,\mathrm{d}t$, $P_A^\tau = \int_0^{T_\mathrm{c}} F_A^\tau(t)\,\mathrm{d}t$.

We designate that $\dot{\delta}_A^+$ is the solution of the impact when ignoring the effects of the non-contact forces. The comparison between $\dot{\delta}_A^+$ and $\dot{\tilde{\delta}}_A^+$ leads to an equality: $(\dot{\tilde{\delta}}_A^+ - \dot{\delta}_A^+)/gT_\mathrm{c} = (hc + rs)\dot{\theta}_m^2/g - 1$. By considering that the value of $\dot{\tilde{\delta}}_A^+$ should be equal to zero in the case of closed contact, the transition from an impact to a contact state is related to a condition

$$\frac{\dot{\delta}_A^+}{gT_\mathrm{c}} = 1 - \frac{(hc + rs)\dot{\theta}_m^2}{mg} < 1. \tag{2.37}$$

The Painlevé paradox is a singularity from the incompatibility between Coulomb's friction law and a complete rigid-body model. To investigate the paradox involved in the slip motion of the disc, let us suppose that the disc slides on the ground with a contact at point A, and $v_A^\tau > 0$. Together with the slide condition in Coulomb's friction, equation (2.35) can be further expressed as

$$\ddot{\delta}_A = \mathbb{A}F_A^n + \mathbb{B}, \tag{2.38}$$

where

$$\mathbb{A} = \frac{1}{m_\mathrm{d}} + \frac{l^2}{2I}(1 + \cos 2(\theta + \varphi)) + \frac{\mu_A l^2}{2I}\sin 2(\theta + \varphi) \tag{2.39}$$

and

$$\mathbb{B} = l\sin(\theta + \varphi)\dot{\theta}^2 - g, \tag{2.40}$$

$l = \sqrt{r^2 + h^2}$ and $\tan\varphi = h/r$.

From (2.19) and (2.38) $l = \sqrt{r^2 + h^2}$ and $\tan\varphi = h/r$. F_A^n is the solution of the linear complementarity problem: $F_A^n \geq 0$, $\ddot{\delta}_A \geq 0$, $F_A^n \cdot \ddot{\delta}_A = 0$. Nevertheless, if $\mathbb{A} < 0$, the Painlevé paradox appears in the system because either no reasonable solution or multiple solutions can be found for the normal contact force. Because the coefficient $\mathbb{A}$ is only affected by the configuration of the system and the value of μ_A, we could directly deduce the condition for the occurrence of the Painlevé paradox by analysing the components of $\mathbb{A}$. Taking into consideration that $(\theta + \varphi) \in [\varphi, \pi/2 + \varphi]$, one finds that $\mathbb{A} < 0$, only if

$$\mu_A \geq -\frac{2I + m_\mathrm{d}l^2(1 + \cos 2(\theta + \varphi))}{m_\mathrm{d}l^2\sin 2(\theta + \varphi)}. \tag{2.41}$$

Equation (2.41) gives the lower bound of μ_A needed for the occurrence of the Painlevé paradox in the disc with a configuration θ. Approximately, this lower bound reaches a minimum value

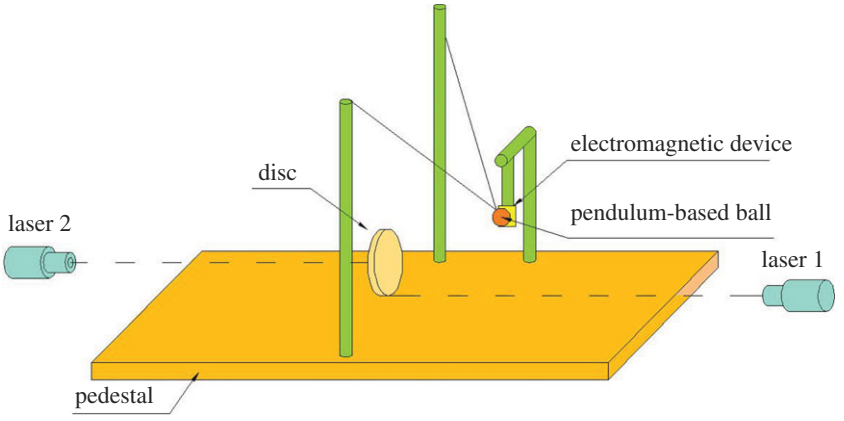

Figure 2. Schematic of experimental apparatus for the disc–ball system. (Online version in colour.)

when $\theta = \pi/2$. With the expression of the moment of inertia, $I = \frac{1}{4}m_d r^2 + \frac{1}{3}m_d h^2$, the minimum value of μ_A at $\theta = \pi/2$ is given by

$$\mu_A\,|_{\min,\theta=\frac{\pi}{2}} = \frac{1}{4}\left(\frac{r}{h}\right) + \frac{4}{3}\left(\frac{h}{r}\right). \tag{2.42}$$

From (2.42), we can find an interesting connection between the minimum value of μ_A and the geometric shape of the disc. The singularity is more easily triggered if the disc takes a shape with a ratio of $r/h = 4\sqrt{3}/3$. In this case, the minimum value of the dynamic coefficient of friction is $\mu_A\,|_{\min} = 2\sqrt{3}/3$. For general materials, it is still an unrealistic value, so we can claim that no Painlevé paradox occurs in the disc–ball system.

If both $\mathbb{A}$ and $\mathbb{B}$ are positive, equation (2.38) indicates that $\ddot{\delta}_A$ cannot stay zero, so that a detachment occurs. The occurrence of the detachment can be determined by the condition $\mathbb{B} > 0$, which corresponds to the following inequality:

$$\dot{\theta}^2 > \frac{g}{l\sin(\theta+\varphi)}. \tag{2.43}$$

The result in equation (2.43) demonstrates that, as the disc approaches the ground, the critical angular velocity required by a detachment increases, and converges to infinity when $\theta \approx 0$. So, we can say that no detachment exists as the disc collapses under gravity.

3. Experimental apparatus, measurement methods and parameters in impact and friction

(a) Experimental apparatus

Figure 2 depicts a schematic of the experimental apparatus, which consists of a pedestal, a pendulum-based steel ball and a steel disc. The disc, pendulum-based ball and pedestal are fabricated from the same stainless steel. An electromagnet device is used to trigger the motion of the ball. The pedestal is a steel plate with four adjustable bolts at its bottom to provide a horizontal plane. The pendulum-based ball is hung from two lines, which are tied on two posts, to make a V shape. The disc stationarily rests on the surface of the pedestal at the position with a line contact located in the plane of the motion of the pendulum-based ball. The impacted surface of the disc is spaced from the bottom of the pendulum by a radius of the ball apart, so that when not in motion, the ball is touching the symmetry axis of the impacted surface of the disc, but no forces occur between them.

Table 1. Material parameters for the ball and the disc.

	mass (g)	radius (mm)	thickness (mm)	Y (GPa)	ν
ball	$m_b = 69.24$	$r_b = 12.5$	/	$Y_s = 206$	$\nu_s = 0.3$
disc	$m = 209.69$	$r = 37.5$	$2h = 6$	$Y_p = 1.20$	$\nu_p = 0.3$

Table 2. Nine cases for experiments of the ball colliding against the disc.

case no.	b (mm)	$\tilde{b} = b/r$	v_b (m s^{-1})
case 1	0	0	0.292
case 2	2.0	0.053	0.275
case 3	4.5	0.12	0.285
case 4	6.5	0.173	0.284
case 5	9.5	0.253	0.433
case 6	15.5	0.413	0.311
case 7	18.5	0.493	0.305
case 8	−2.5	−0.067	0.353
case 9	−6.5	−0.173	0.293

The pendulum lines are strung to the ball via a small metal tube welded on the top of the ball, and are stiff enough to balance the centripetal force experienced by the ball as it travels down along an arc. Initially, the striker ball is attracted to the electromagnet owing to the electromagnetic force. By switching off the circuit connecting to the electromagnet, the ball is released, and travels down the arc through a small distance, then strikes normally the stationary disc at the bottom of the arc. The position of the electromagnet is held by a track, which can be removed vertically to provide various heights, so that different impact velocities at different impact points between the ball and the disc can be achieved by changing the length of the pendulum lines.

When an impact between the ball and the disc occurs on a steel–steel surface, we found that high-frequency noise is triggered, which then significantly influences the friction property on the line contact. In order to eliminate these effects, a three-ply detective paper fabricated from phenolic material is glued on the impacted surface of the disc. The related material parameters are listed in table 1, in which the material property of phenolics is directly applied into the contact mechanics related to the impacted surface of the disc.

(b) Measurement methods

The velocities of the ball and the disc before and after collision were measured using two laser-Doppler vibrometers (Polytec-OFV-3001-353). The instantaneous velocity of the moving point along the direction of the laser beam was captured by an analogue-to-digital card (PMD-1608FS) with a sample rate 50 kHz. In order to guarantee laser lines parallel to the horizontal surface, we set a mirror perpendicular to the horizontal pedestal surface, then adjusted the laser head to make the laser beam reflect back to its origin. By changing the length of the pendulum string and adjusting the height of the electromagnet, experiments were carried out by setting the moving ball with nine different incident conditions relating to the incident velocity v_b and the impact position b (table 2). The negative value of b represents an impact position below the mass centre of the disc, while a positive value represents an impact position above the mass centre. For all experiments, the two laser sensors were fixed at heights $h_1 = 4$ mm and $h_2 = 37.5$ mm with an uncertainty interval $[-0.05, 0.05]$ mm.

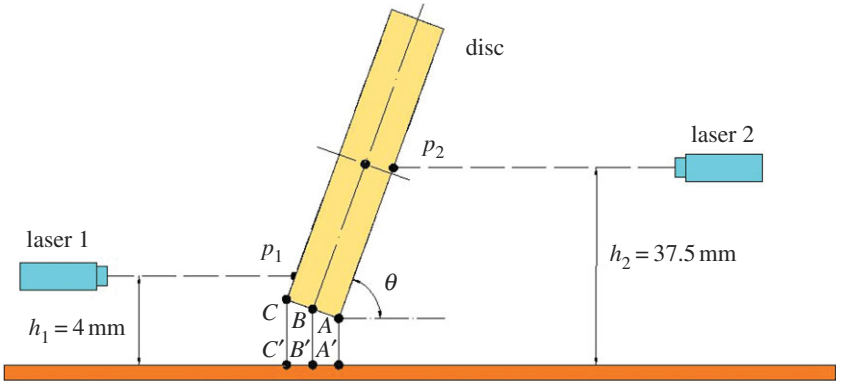

Figure 3. Measurement of the two-dimensional motion of the disc using two laser beams. (Online version in colour.)

For a given experiment, we first remove the disc from the horizontal surface, then use laser 2 to measure the incident velocity of the ball by releasing it from a selected height. This procedure is repeated 10 times to achieve a stable value. Once the incident velocity of the ball and the impact position are assumed to be correctly determined, we put the disc on the horizontal surface at the correct site calibrated by laser sensors, and start the experiment using laser sensors to capture the velocities of the disc. Repeatability error is checked by carrying out five trials for each set of experiments.

The principle of the measurements is shown in figure 3, in which two laser lines are parallel to the horizontal surface, and intersect the corresponding surfaces of the disc at two measured points p_1 and p_2 over the ground with vertical heights h_1 and h_2, respectively. Both points are at different locations on the disc surfaces from time to time, but the measured values of $v_1^p(t)$ and $v_2^p(t)$ from two laser sensors follow the relationship

$$v_2^p(t)\boldsymbol{j} = v_1^p(t)\boldsymbol{j} + \dot{\theta}^p(t)\boldsymbol{i} \times (h_2 - h_1)\boldsymbol{k} = (v_1^p(t) - \dot{\theta}^p(t)(h_2 - h_1))\boldsymbol{j}. \tag{3.1}$$

Then, the angular velocity $\dot{\theta}^p(t)$ of the disc at the instant t can be calculated using $\dot{\theta}^p(t) = -(v_1^p - v_2^p)/(h_1 - h_2)$. The initial configuration of the disc $\theta(t_0) = \pi/2$ allows the measured value for the angle to be expressed as $\theta^p(t) = \pi/2 - 1/(h_1 - h_2)\int_{t_0}^{t}(v_1^m(t) - v_2^m(t))\,\mathrm{d}t$.

To compare the numerical simulation and experimental data, we use the following expressions to provide the numerical results for the horizontal velocities at the two measured points:

$$\left.\begin{aligned} v_1^N(t) &= \dot{y}_\mathrm{d}^N(t) + (z_\mathrm{d}^N(t) - h_1)\dot{\theta}^N(t) \\ \text{and} \quad v_2^N(t) &= \dot{y}_\mathrm{d}^N(t) + (z_\mathrm{d}^N(t) - h_2)\dot{\theta}^N(t). \end{aligned}\right\} \tag{3.2}$$

(c) Coefficient of restitution

The coefficient of restitution is crucial for numerical simulations. Nevertheless, its value cannot be thought of as constant when friction is involved in impacts, or multiple impacts are presented. To elude the influence of the line contact on the impact, we set $b = 0$ to trigger a normal collision between the disc and the ball. In this case, the energetic coefficient of restitution agrees with Newton's kinematic coefficient of restitution, which can be experimentally determined by

$$e_D = -\frac{v_\mathrm{b}^{n,+} - v_\mathrm{d}^{n,+}}{v_\mathrm{b}^{n,-} - v_\mathrm{d}^{n,-}} = -\frac{v_2^p - v_1^p}{v_\mathrm{b}}, \tag{3.3}$$

where $v_{\mathrm{b}}^{n,+} = v_2^p$ and $v_{\mathrm{d}}^{n,+} = v_1^p$ are the post-impact velocities of the ball and the disc after impacts, captured by two laser sensors. Equality $v_{\mathrm{d}}^{n,+} = v_1^p$ exists in the disc without rotation, and $v_{\mathrm{b}}^{n,-} = v_{\mathrm{b}}$ is the incident velocity of the ball.

Owing to the change of the material property (from elasticity to plasticity), lots of studies demonstrated that the coefficient of restitution, even in a normal collision, is affected by the impact velocity [5,15]. For the experiments in this paper, however, the impact velocity is very low and confined to a limited scope, such that its value can be assumed to be a material-dependent parameter localized in the impact region. Under the assumption, the coefficients of restitution for all the points in the line contact take the same value obtained from the experiment (case 1) of letting the ball normally collide against the disc centre on a steel–steel surface. The coefficient of restitution for point D is identified by a similar normal impact experiment that occurs on a paper–steel surface. For the two kinds of normal impacts occurring at different impacted surfaces, we carry out 15 trials for each set of experiments, and find good repeatability.

(d) Coefficient of friction

Despite that friction parameters mainly depend on the material properties of the contacting bodies, their values often change with a dynamics process. To compare numerical results with experiments as precisely as possible, we identify the values of friction coefficients using the experimental data related to case 2, in which the post-impact motion of the disc reveals typical frictional behaviours, including a continuous slip, stick-to-slip transition, and vice versa.

In terms of the measured values $v_1^p(t)$ and $v_2^p(t)$ in case 2, we obtain the time histories of $v_A^{\tau,p}(t)$ (figure 4*a*) and $\dot{\theta}^p$ (whose picture is omitted), then respectively perform differential and integral operations to obtain $\dot{v}_A^{\tau,p}$ and θ^p. Under the condition that the disc is in contact with the plate after impact, we set equation (2.15) equal to zero for the normal motion of the contact point, and combine it with equation (2.16) (the tangential motions of the contact point), to get the equations whose unknown quantities only include the normal and tangential forces $F_A^n(t)$ and $F_A^\tau(t)$. Together with the values obtained from experimental data, we can calculate $F_A^n(t)$ and $F_A^\tau(t)$, then obtain the ratio, $\mu = F_A^\tau / F_A^n$ (figure 4*b*). Observations from figure 4*a*,*b* clearly demonstrate that the ratio, $\mu = F_A^\tau / F_A^n$, approaches a constant in the slip motion of the contact point, while its value varies dramatically in the stick state, and arrives at a maximum once slip resumes. We assign the value in the slip state to the slip coefficient of friction, and the maximum in the stick state to the stick coefficient of friction.

By fixing these values in other cases, except cases 5 and 6, we will show that good agreement between numerical and experimental results are obtained. The exceptions of the friction coefficients in cases 5 and 6 are due to the variation of the contact surfaces. The two experiments were supplemented for verifying certain special phenomena, which were found in a comprehensive numerical investigation that was carried out at a time when most of the experimental work had been finished for a long time.

The suppression of the impact-agitated high-frequency noise makes a stable property for the friction between the disc and the rough ground. Nevertheless, the identified value of the stick coefficient seems to be smaller than the ones given in material manuals. We explain this anomalous phenomenon as follows: the motion of the disc in our experiments is localized at a very small contact area, which is very different to the conventional scenario of friction experiments, in which a flat face is usually involved. By considering that slip motion essentially originates from the failure of the material on a bulk of asperities, the narrow contact region around a geometrical point may not allow a large difference between slip and stick coefficients. This may be the reason why, in our experiments, the stick coefficient exceeds the slip one by only a small value. Paper addition at point D smoothes the interface with low friction. We estimate μ_D and μ_D^{s} with the half value of the respective ones of the slip and stick coefficients of friction measured for the line contact.

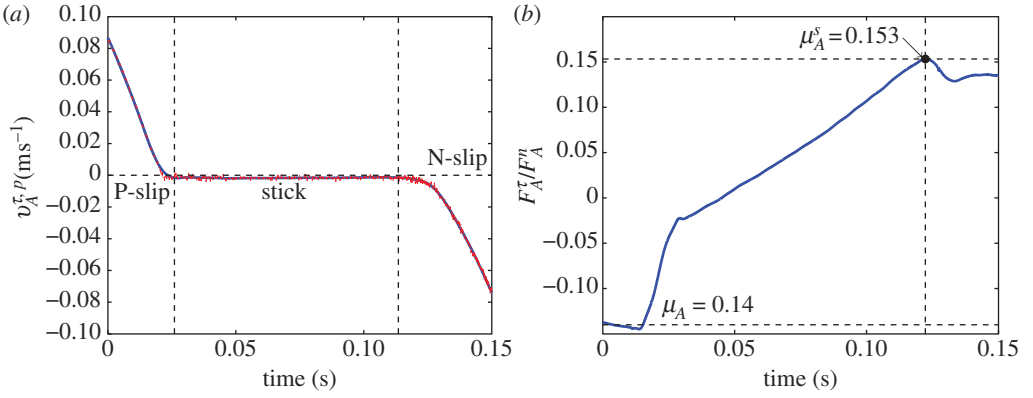

Figure 4. (*a*) Tangential velocity $v_A^{\tau,p}$ in case 2 (the dashed line represents the raw data in experiments, and the solid line refers to the data smoothed using the 20-point method in MATLAB for data processing). (*b*) Value of F_A^τ/F_A^n obtained from the experiment in case 2. (Online version in colour.)

(e) Compliance model at contact points

Impact dynamics requires a constitutive model for each contact point, even though local small deformation is successfully eluded by using a differential normal impulse as a substitution for time. To simplify, we assume that the normal contact forces at all the points approximately satisfy the relationship of a Hertzian model [33],

$$F_i^n = k_i \delta_i^{3/2}, \quad i = A, B, C, D, \tag{3.4}$$

where k_i is the contact stiffness. For the contact at point D, similar to a sphere contacting with a flat face, the contact stiffness is easily given by $k_D = (4E_D^*/3)\sqrt{r_b}$, where $E_D^* = (1-\nu_s^2)/E_s + (1-\nu_p^2)/E_p$ is the equivalent elastic modulus. We approximately think of the point contact in the line as a planar stress problem, similar to a slice with radius r contacting an elastic half-infinite space. So the contact stiffness for these points is expressed as $k_i = (4E_i^*/3)\sqrt{r}$, $i = A, B, C$, where $E_i^* = 2(1-\nu_s^2)/E_s$.

4. Numerical and experimental investigations

Table 3 presents model parameters identified from experiments or calculated using material properties. In this section, we use these model parameters to perform numerical investigations for all cases tested in the experiments, then present comparisons between numerical and experimental results to illustrate the complex behaviour of the disc generated by impacts.

(a) Comparisons for the results in impact dynamics

With the material and model parameters shown in tables 1 and 3, we choose the explicit Euler differential method to solve the differential impulsive equations. The primary normal impulse P_j^n is assigned to the point with the maximum potential energy among various points, and the time step is $\triangle P_j^n = m v_b/N$, $N = 10^4$. The impact at a single point finishes when no potential energy resides on the point, and the whole scenario of the impacts ends if the potential energies at all contact points are completely released.

In experiments, the laser sensors with a sample rate of 50 kHz provide a small time interval for the impacts. In order to compare the numerical and experimental results, we define a characteristic time scale T_c to estimate the time interval experienced by the multiple impacts. Based on numerical investigations, the single impact at point D dominates the dynamics. We suppose that the value of T_c is characterized by the time interval experienced by a single normal

Table 3. Model parameters of contact points for nine experimental cases.

point	e_i	μ_i^s	μ_i	k_i (N m^{-1})	case no.
D	0.7043	0.075	0.07	1.9640×10^8	1–9
A, B, C	0.9064	0.15	0.14	2.9217×10^{10}	1–4, 7–9
A, B, C	0.9064	0.23	0.185	2.9217×10^{10}	5
A, B, C	0.9064	0.23	0.17	2.9217×10^{10}	6

Table 4. Comparison between numerical and experimental results relating the post- horizontal velocities at two measuring points after impacts. $(\cdot)_{(\cdot)}^{p,+}$, The mean values obtained from five experimental trials; $(\cdot)_{(\cdot)}^{N,+}$, the numerical results.

	case 2	case 3	case 4	case 5
$v_1^{p,+}$	$0.0895 \pm {}^{0.0020}_{0.0022}$	$0.0625 \pm {}^{0.0006}_{0.0014}$	$0.0415 \pm {}^{0.0030}_{0.0012}$	$0.0194 \pm {}^{0.0017}_{0.0013}$
$v_1^{N,+}$	0.0918	0.0660	0.0427	0.0184
$\dot{\theta}^{p,+}$	$-0.6324 \pm {}^{0.0172}_{0.0303}$	$-1.5985 \pm {}^{0.0332}_{0.507}$	$-2.1750 \pm {}^{0.0364}_{0.0681}$	$-4.5613 \pm {}^{0.1096}_{0.0439}$
$\dot{\theta}^{N,+}$	−0.7208	−1.5743	−2.2012	−4.5943
$v_2^{p,+}$	$0.1095 \pm {}^{0.0017}_{0.0020}$	$0.1142 \pm {}^{0.0018}_{0.0017}$	$0.1135 \pm {}^{0.0020}_{0.0010}$	$0.1722 \pm {}^{0.0021}_{0.0027}$
$v_2^{N,+}$	0.1160	0.1188	0.1166	0.1725
	case 6	case 7	case 8	case 9
$v_1^{p,+}$	$-0.0796 \pm {}^{0.0057}_{0.0042}$	$-0.0485 \pm {}^{0.0003}_{0.0029}$	$0.1733 \pm {}^{0.0006}_{0.0008}$	$0.1683 \pm {}^{0.0041}_{0.0033}$
$v_1^{N,+}$	−0.0559	−0.0521	0.1750	0.1670
$\dot{\theta}^{p,+}$	$-6.0726 \pm {}^{0.2424}_{0.1481}$	$-4.6367 \pm {}^{0.0863}_{0.1161}$	$0.9205 \pm {}^{0.0136}_{0.1171}$	$1.6234 \pm {}^{0.0822}_{0.0130}$
$\dot{\theta}^{N,+}$	−5.4828	−4.7004	0.8854	1.7274
$v_2^{p,+}$	$0.1206 \pm {}^{0.0038}_{0.0025}$	$0.1025 \pm {}^{0.0012}_{0.0010}$	$0.1413 \pm {}^{0.0014}_{0.0007}$	$0.1143 \pm {}^{0.0012}_{0.0022}$
$v_2^{N,+}$	0.1280	0.1056	0.1453	0.1170

impact between the disc and the ball. Under this assumption, the value of T_c can be expressed as [33]

$$T_c = 2.87 \left(\frac{m^{*2}}{r_b E_D^{*2} v_b} \right)^{1/5} = k_{T_c} (v_b)^{-1/5}, \tag{4.1}$$

where $m^* = m_b m_d/(m_b + m_d)$ and $k_{T_c} = 4.7531 \times 10^{-4} (\mathrm{m}^{-1/5}\mathrm{s}^{4/5})$ according to the material parameters of the system. For the incident velocities of the ball concerned, T_c is approximately 0.1 ms. Under the sampling rate 50 Hz, the experimental data confined in an impact process contain five discrete values. For each experimental trial, we sample the value at the fifth point as the output of the impact, and average the values obtained from five trials to determine the outputs for each case investigated. Table 4 presents the mean values of the experimental results, together with the uncertainty interval that corresponds to the minimum and maximum measured values. The relative error less than 5 per cent for any case shows good agreement between numerical and experimental results.

(b) Post-impact patterns of the contact states

Impact dynamics provide post-impact states to initialize the subsequent motion of the disc. Owing to the geometrical limitation from the ground, the points in the line contact after impact may either hold in sticking or slipping on the ground, or be airborne, thus enriching the dynamic behaviour of the disc. To characterize the impact-generated patterns of the disc, we define

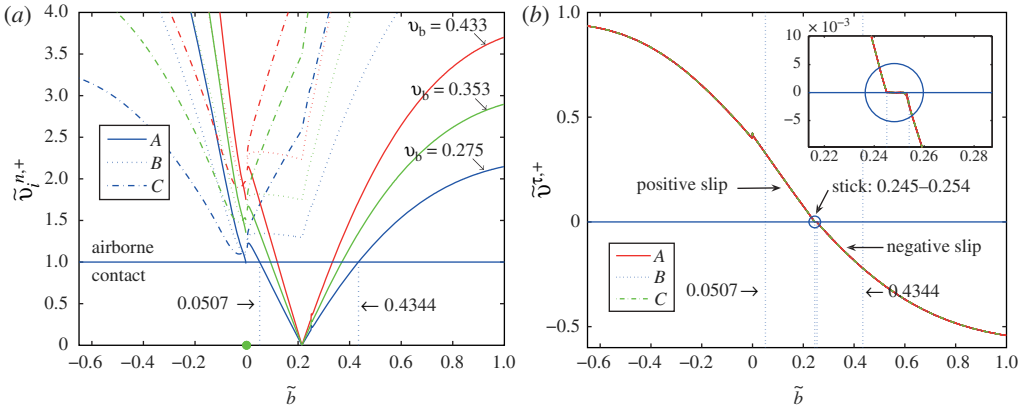

Figure 5. (*a*) Dimensionless normal velocities and (*b*) dimensionless tangential velocities, for points *A*, *B* and *C* at the end of the impacts. The inset in (*b*) demonstrates that there exists a region related to the tangential velocity vanishing. (Online version in colour.)

the following dimensionless variables: $\tilde{b} = b/r$, $\tilde{\upsilon}_i^{n,+} = \upsilon_i^{n,+}/gT_c$, $\tilde{\upsilon}_i^{\tau,+} = \upsilon_i^{\tau,+}/\upsilon_b$, $\tilde{\dot{\theta}}^+ = r\dot{\theta}^+/\upsilon_b$, $i = A, B, C$. Variable $\tilde{b}$ is used to reflect the effects of impact position on the post-impact states of the disc, $\tilde{\upsilon}_i^{n,+}$ is defined for distinguishing the normal state of point i (see (2.37)), $\tilde{\upsilon}_i^{\tau,+}$ for the tangential state related to the point in contact with the ground, and $\tilde{\dot{\theta}}^+$ for the rotation of the disc.

By altering the impact position within an interval $\tilde{b} \in [-0.6, 1]$, we carry out numerical investigations by letting the ball take incident velocities with the values in cases 2, 5 and 8, respectively. Figure 5*a* presents the value of $\tilde{\upsilon}_i^{n,+}$ versus $\tilde{b}$. Around the vicinity of the disc centre, we find $\tilde{\upsilon}_i^{n,+} = 0$, which corresponds to a single normal impact in the case $\tilde{b} = 0$. When $\tilde{b} < 0$, the disc cannot hold on the ground after impact since we always have $\tilde{\upsilon}_i^{n,+} > 1$. In the case $\tilde{b} > 0$, there exists a region for the impact positions that make $\tilde{\upsilon}_A^{n,+} < 1$, so that the disc after the initial impact can stay in contact with the fixed surface. With the increase of υ_b, the region of the impact position that can keep the disc in contact with the ground shrinks a little, and always contains a fixed point located approximately at a value $\tilde{b} \approx 0.21$. This impact position is similar to a central shock that allows point *A* to be insensitive to the impact.

The values of $\tilde{\upsilon}_i^{\tau,+}$ are shown in figure 5*b*, which fully overlap each other for the impact at the same impact position with different values of υ_b. Combining figure 5*a* with figure 5*b* indicates that there is a narrow region in which the disc can hold a stick state on the ground (see the inset in figure 5*b*). Meanwhile, we also find that the sign of $\tilde{b}$ features the rotation direction of the disc after impact: if $\tilde{b} > 0$, the post-impact rotation of the disc takes a counter-clockwise direction, and the direction is reversed when $\tilde{b} < 0$.

To characterize the post-impact patterns of the contact states of the disc, we specify six modes, as shown in table 5, in association with the corresponding intervals of $\tilde{b}$, whose boundaries are related to the results obtained from $\upsilon_b = 0.275\,\mathrm{m\,s^{-1}}$. The symbols in table 5 are defined as follows: NC, the point separates from the ground; SP, the point takes a state in contact with a positive slip motion; SN, the point remains as a negative slip motion; ST, the point sticks to the ground. The last column in table 5 lists the case numbers of the experiments relevant to a specific mode.

(c) Subsequent motion of the disc

Once the initial impact is solved, no complexity generally is involved in such a simple object. Nevertheless, investigations for the subsequent motion of the disc present an intuitive way to verify the results obtained from impact dynamics. For the cases tested as shown in table 2, we fix the parameters in table 3, and perform numerical simulations using the values listed in table 4 as

Table 5. Impact-generated patterns for motion of the disc after impact. NC, the point separates from the ground; SP, the point takes a state in contact with a positive slip motion; SN, the point remains as a negative slip motion; ST, the point sticks to the ground.

mode no.	impact position $\tilde{b}$	A	B	C	$\dot{\tilde{\theta}}^+$	exp. no.
I	$\tilde{b} < 0$	NC	NC	NC	$\dot{\tilde{\theta}}^+ > 0$	8, 9
II	$\tilde{b} = 0$	SP	SP	SP	$\dot{\tilde{\theta}}^+ = 0$	1
III	$\tilde{b} \in (0, 0.0507] \bigcup (0.4344, 1]$	NC	NC	NC	$\dot{\tilde{\theta}}^+ < 0$	7
IV	$\tilde{b} \in (0.0507, 0.244]$	SP	NC	NC	$\dot{\tilde{\theta}}^+ < 0$	2,3,4
V	$\tilde{b} \in (0.244, 0.254]$	ST	NC	NC	$\dot{\tilde{\theta}}^+ < 0$	5
VI	$\tilde{b} \in (0.254, 0.4344]$	SN	NC	NC	$\dot{\tilde{\theta}}^+ < 0$	6

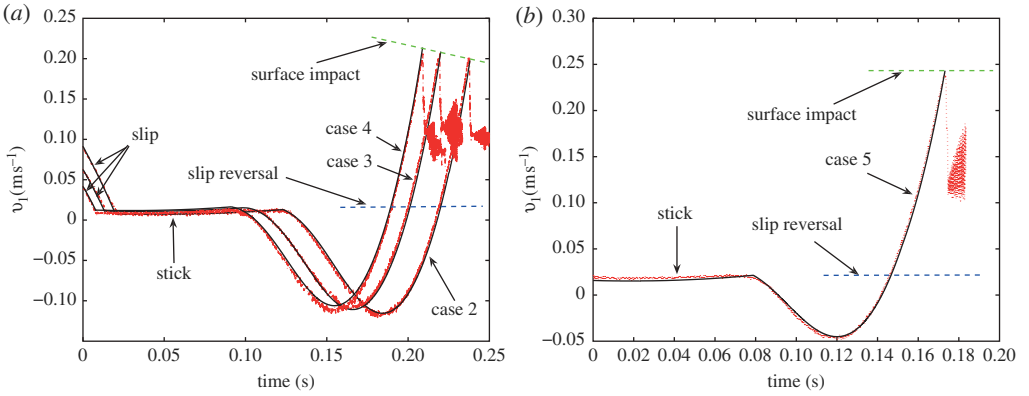

Figure 6. Comparisons between numerical and experimental results for the velocity of the gauged point p_1 in (*a*) cases 2, 3, 4 (dashed-dotted line represents experiment and solid line represents simulation) and (*b*) case 5 (dotted line represents experiment and solid line represents simulation). (Online version in colour.)

the initial conditions for the subsequent motion of the disc. The comparisons between numerical and experimental results are directly based on the horizontal velocities at the measured position p_1. We select the best one as the experimental curves plotted in figures 6–8.

Because the point p_1 is slightly apart from the ground, the measured velocity is very close to the tangential velocity of the contact point, such that the contact states between the disc and the ground are well reflected by the experimental curves. The stick–slip behaviour is distinguished by directly inspecting the values in the curves, while the detachment of the disc is recognized by the occurrence of steps in the curves, which result from a sequence of single impacts.

Figure 6*a* presents the horizontal velocities at point p_1 in cases 2, 3 and 4. In these cases, the subsequent motions are initialized by mode IV, where the disc is in contact with the ground after the ball collides against the disc. Therefore, the disc starts a continuous slip motion until the tangential velocity vanishes, then sticks for a while, after that a slip motion resumes in a reverse direction to its first slip phase. The resumed slip motion will be immediately transferred into a positive slip once the tangential velocity disappears again.

Figure 6*b* shows the horizontal velocities at point p_1 in case 5, in which the subsequent motion starts with mode V, where point A is initialized by the ball impact with a stick state. In this case, the disc firstly rotates around point A, then a transition from stick to slip is triggered owing to the increase of the inertial force that changes the frictional behaviour at contact point A. After that, the motion of the disc takes similar frictional behaviour to cases 2, 3 and 4.

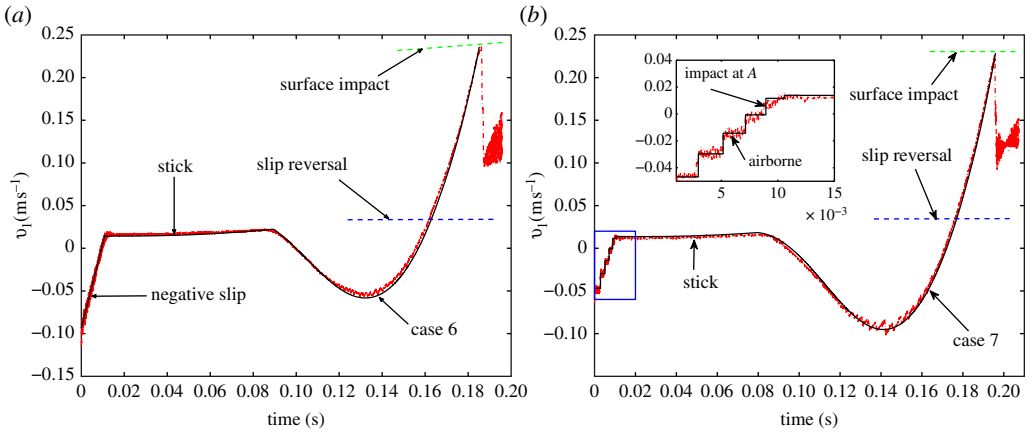

Figure 7. Comparisons between numerical and experimental results for the velocity of the gauged point p_1 in (*a*) case 6 and (*b*) case 7. Dashed-dotted line represents experiment and solid line represents simulation. (Online version in colour.)

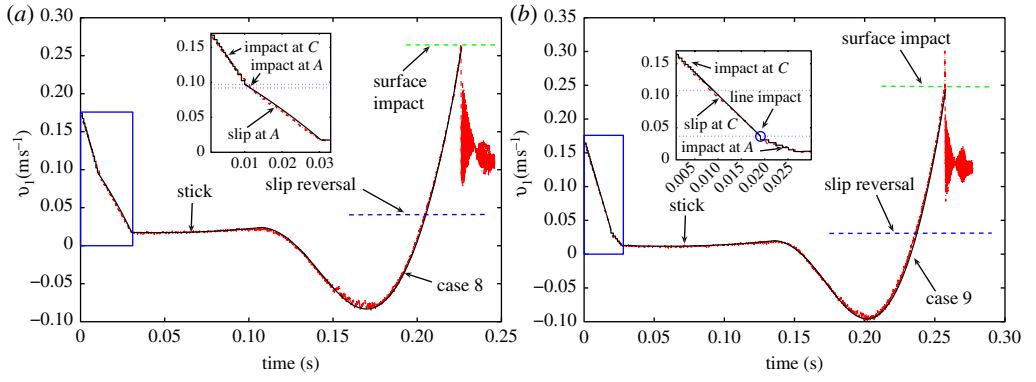

Figure 8. Comparisons between numerical and experimental results for the velocity of the gauged point p_1 in (*a*) case 8 and (*b*) case 9. The inset in (*a*) demonstrates that the sequence of impacts at point *C* is transferred into a sequence of impacts at point *A*. The inset in (*b*) reveals that a line impact is involved in the subsequent motion of the disc. Dashed-dotted line represents experiment and solid line represents simulation. (Online version in colour.)

In figure 7*a*, numerical simulation and experimental data show that the post-impact state of the disc in case 6 is in mode VI, where a negative slip motion is initiated by the initial impact of the ball. In this case, the subsequent motion consists of four phases, including a negative slip motion, a stick motion after a stick–slip transition, a negative slip motion and a positive slip motion.

Figure 7*b* demonstrates that case 7 brings the disc into mode III, where the disc detaches from the ground after the initial impact. Thus, a sequence of single impacts appears in its subsequent motion. These discrete impact events result in discontinuous curves characterized by a sequence of steps in its first process. The intensity of the single impact decreases owing to the energy dissipation, and the jump motion of the disc is stabilized by a stick contact state. Then, a similar contact behaviour as shown in other cases appears.

Figure 8*a*,*b* confirm that cases 8 and 9 are involved in mode I, when the impact position is below the centre of the disc. In this impact-generated mode, the disc cannot hold a contact on the ground after the impact from the ball. Therefore, the first phase for the subsequent motion is free, and the disc will return back to collide against the ground at point *C*. Despite the main characteristics being the same in the two cases, slight differences in the evolutions of their subsequent dynamics can be observed. In case 8, the sequence of single impacts at point *C* is transferred into a sequence

of impacts at point A, followed by a slip motion. In case 9, the sequence of single impacts at point C is firstly transferred into a slip motion, then followed by a line impact ($\theta = \pi/2$) to trigger a slip motion at point A.

For all the cases tested, a surface impact is triggered at the final stage of the disc motion, and excites a high-frequency vibration. Regardless of the surface impact, the theoretical model can precisely reproduce all the complex phenomena, consisting of a sequence of frictional impacts, transitions among stick–slip motions and the impact–contact switches, as well as a line impact. Interestingly, even though the initial states are very different to each other, the subsequent motion of the disc seems to be stabilized by a stick state, then converges to a similar dynamical behaviour.

5. Summary and conclusions

The main conclusions and developments of this paper are summarized as follows.

— We deal with a contact–impact problem in a uniform framework that encapsulates different structures of the mathematical model, including contacts, impacts, stick–slip in friction and transitions among different states of the variable-structure dynamics.
— We present our previous theory of multiple impacts in a more concise way, and extend it to the cases with friction. A concept of efficiency of energy transition is proposed to reflect the dissipation of energy that, in a single full compression–expansion cycle, agrees with the definition of the energetic coefficient of restitution.
— The transitions among different structures in the mathematical model are quantified by legible conditions without ambiguities.
— We discuss the problem of the Painlevé paradox in the disc–ball system and present some theoretical results.

To verify our theoretical results, an experimental setup associated with the disc–ball system was built, a measurement technique using two laser vibrometers to perform experimental observations was developed, and the model parameters crucial to simulations were correctly identified. Without any artificial parameters obtained from an arbitrary fitting process, we obtained excellent agreement between the numerical and experimental results for the whole scenario of the dynamics, including the initial impacts and the subsequent motion of the disc. Our results not only justify the proposed theory, but also demonstrate that such a simple system exhibits rich patterns generated by impacts with friction. These phenomena suggest that the energy residing on interfaces, which is of a small magnitude and evolves rapidly, manifests a prominent role for the gross motion of systems. This point may have implications in understanding the complex behaviour of systems subject to dry friction.

This work was performed with the support of the NSFC key project (11132001).

References

1. Glocker Ch, Pfeiffer F. 1995 Multiple impacts with friction in rigid multibody systems. *Nonlinear Dyn.* **7**, 471–497. (doi:10.1007/BF00121109)
2. Ivanov AP. 1995 On multiple impacts. *J. Appl. Math. Mech.* **59**, 887–902. (doi:10.1016/0021-8928(95)00122-0)
3. Moreau JJ. 1988 Unilaterial contact and dry friction in finite freedom dynamics. In *CISM nonsmooth mechanics and applications*, vol. 302, pp. 1–82. Vienna, Austria: Springer.
4. Lankarani H, Nikravesh P. 1994 Continuous contact force models for impact analysis in multibody systems. *Nonlinear Dyn.* **5**, 193–207.
5. Stronge WJ. 2000 *Impact mechanics.* Cambridge, UK: Cambridge University Press.
6. Escalona JL, Sany JR, Shabana AA. 2002 On the use of the restitution condition in flexible body dynamics. *Nonlinear Dyn.* **30**, 71–86. (doi:10.1023/A:1020337204996)
7. Brogliato B. 1999 *Nonsmooth mechanics*, 2nd edn. London, UK: Springer.

8. Schiehlen W. 1997 Multibody system dynamics: roots and perspectives. *Multibody Syst. Dyn.* **1**, 149–188. (doi:10.1023/A:1009745432698)
9. Stewart D. 2000 Rigid-body dynamics with friction and impact. *SIAM Rev.* **42**, 3–39. (doi:10.1137/S0036144599360110)
10. Ivanov AP. 2003 Singularities in the dynamics of systems with non-ideal constraints. *J. Appl. Math. Mech.* **67**, 185–192. (doi:10.1016/S0021-8928(03)90004-9)
11. Génot F, Brogliato B. 1999 New results on Painlevé paradoxes. *Eur.J. Mech. A Solids* **18**, 653–677. (doi:10.1016/S0997-7538(99)00144-8)
12. Liu C, Zhao Z, Chen B. 2007 The bouncing motion appearing in a robotic system with unilateral constraint. *Nonlinear Dyn.* **49**, 217–232. (doi:10.1007/s11071-006-9123-z)
13. Painlevé P. 1895 Sur les lois du frottement de glissement. *C.R. Hebd. Séances Acad. Sci. Paris* **121**, 112–115.
14. Zhao Z, Liu C, Ma W, Chen B. 2008 Experimental investigation of the Painlevé paradox in a robotic system. *J. Appl. Mech.* **75**, 041006. (doi:10.1115/1.2910825)
15. Garland PP, Rogers RJ. 2009 An experiment study of contact forces during oblique elastic impact. *J. Appl. Mech.* **76**, 031015. (doi:10.1115/1.3063634)
16. Maw M, Barber JR, Fawcett JN. 1977 The rebound of elastic bodies in oblique impact. *Mech. Res. Commun.* **4**, 17–22. (doi:10.1016/0093-6413(77)90045-3)
17. Falcon E, Laroche C, Fauve S, Coste S. 1998 Collision of a 1-D column of beads with a wall. *Eur. Phys. J. B* **5**, 111–131. (doi:10.1007/s100510050424)
18. Khulief Y, Shabana A. 1987 A continuous force model for the impact analysis of flexible multibody systems. *Mech. Mach. Theory* **22**, 213–224. (doi:10.1016/0094-114X(87)90004-8)
19. Liu C, Zhao Z, Brogliato B. 2008 Frictionless multiple impacts in multibody systems. I. Theoretical framework. *Proc. R. Soc. A* **464**, 3193–3211. (doi:10.1098/rspa.2008.0078)
20. Liu C, Zhao Z, Brogliato B. 2008 Energy dissipation and dispersion effects in a granular media. *Phys. Rev. E* **78**, 031307. (doi:10.1103/PhysRevE.78.031307)
21. Nguyen N, Brogliato B. 2012 Shock dynamics in granular chains: numerical simulations and comparison with experimental tests. *Granular Matter* **14**, 341–362. (doi:10.1007/s10035-012-0338-z)
22. Zhao Z, Liu C, Brogliato B. 2009 Planar dynamics of a rigid body system with frictional impacts. II. Qualitative analysis and numerical simulations. *Proc. R. Soc. A* **465**, 2267–2292. (doi:10.1098/rspa.2008.0079)
23. Darboux G. 1880 Etude géométrique sur les percussions et le choc des corps. *Bulletin des Sciences Mathématiques et Astronomiques Deuxième Série* **4**, 126–160.
24. Keller JB. 1986 Impact with friction. *J. Appl. Mech.* **53**, 1–4. (doi:10.1115/1.3171712)
25. Bhatt V. 1995 Three-dimensional frictional rigid-body impact. *J. Appl. Mech.* **62**, 893–898. (doi:10.1115/1.2896017)
26. Nordmark A, Dankowicz H, Champneys A. 2009 Discontinuity-induced bifurcations in systems with impacts and friction: discontinuities in the impact law. *Int. J. NonLinear Mech.* **44**, 1011–1023. (doi:10.1016/j.ijnonlinmec.2009.05.009)
27. Oded B-D, Rubinstein SM, Jay F. 2010 Slip–stick and the evolution of frictional strength. *Nature* **463**, 76–79. (doi:10.1038/nature08676)
28. Dankowicz H. 1999 On the modeling of dynamics friction phenomena. *Z. Angew. Math. Mech.* **79**, 399–409. (doi:10.1002/(SICI)1521-4001(199906)79:6<399::AID-ZAMM399>3.0.CO;2-K)
29. Eriten M, Polycarpou A, Bergman LA. 2011 Physics-based modelling for fretting behaviour of nominally flat rough surface. *Int. J. Solids Struct.* **48**, 1436–1450. (doi:10.1016/j.ijsolstr.2011.01.028)
30. Eriten M, Polycarpou A, Bergman LA. 2012 A physics-based friction model and integration to a simple dynamical system. *J. Vib. Acoust.* **134**, 051012. (doi:10.1115/1.4006182)
31. Jia YB. 2013 Three-dimensional impact: energy-based modeling of tangential compliance. *Int. J. Robot. Res.* **32**, 56–83. (doi:10.1177/0278364912457832)
32. Jia YB, Matthew TM, Michael AE. 2012 Multiple impacts: a state transition diagram approach. *Int. J. Robot. Res.* **32**, 84–114. (doi:10.1177/0278364912461539)
33. Johnson KL. 1992 *Contact mechanics*. Cambridge, UK: Cambridge University Press.